nature communications

Article

https://doi.org/10.1038/s41467-025-64418-7

Low-coordinated Co-Ru dual-atom enables ambient ammoxidation via unlocking competitive adsorption limitations

Received: 24 February 2025

Accepted: 12 September 2025

Published online: 22 October 2025

Check for updates

Jialin Yang[1,6], Zhecheng Fang[2,6], Zhiwei Sun[1,6], Wenhua Zhou[2], Bing Nan[3] ✉, Xiaolong Liu[4] ✉, Zixu Ma[1], Renfeng Nie[1] ✉ & Jie Fu[2,5] ✉

Direct ammoxidation of biomass-derived alcohols/aldehydes to nitriles faces challenges from N-species competitive adsorption, leading to low efficiency under harsh conditions. Herein, we report the rational design of a single-nitrogen-bridged Co-Ru dual-atom catalyst (CoRu-N-C) on nitrogen-doped carbon, enabling efficient ammoxidation at ambient conditions. At 35 °C and 1 bar air, CoRu-N-C achieved 98% yield of 2-furonitrile (FAN) with 73 mmol/$g_{\text{-metal}}$/h productivity, representing a 3.5-fold enhancement compared to Co-N-C, and outperforming numerous reported noble/non-noble metal catalysts. Mechanistic studies reveal synergistic O_2 and imine adsorption on low-coordinated CoN_3 and RuN_3 sites, mitigating imine-induced oxygen activation inhibition. Specifically, the strong O_2 adsorption on CoN_3 forms superoxide radicals ($O_2^{-\bullet}$) via electron transfer, driving a relay mechanism with proximally adsorbed imine to accelerate overall reaction kinetics. This work provides valuable insights for the design of stable and highly efficient ammoxidation catalysts operating under mild conditions.

Nitriles serve as essential intermediates in diverse applications spanning medicinal chemistry, organic synthesis, and polymer science[1–3]. Traditional nitrile synthesis methods, including the Sandmeyer[4], Rosenmund-von Braun[5], and cyanation of halogenated alkanes[6], as well as the Wittig reaction[7], often necessitate harsh reaction conditions (high temperatures or pressures) and employ hazardous metal cyanides, thus compromising principles of green chemistry. Consequently, the development of sustainable and atom-economical nitrile synthesis strategies remains a significant challenge.

Biomass, a renewable and carbon-negative resource, offers a sustainable pathway to valuable oxygenated intermediates via pyrolysis, dehydration, or hydrolysis[8,9], providing a compelling alternative to fossil fuel-based feedstocks. A particularly promising approach to sustainable nitrile synthesis involves the catalytic ammoxidation of biomass-derived alcohols and aldehydes using oxygen and ammonia, generating water as the sole byproduct[10]. While homogeneous catalysts, such as copper and iron complexes, have demonstrated catalytic activity[11–13], challenges related to product separation and catalyst recovery persist. Consequently, heterogeneous catalysts, including both noble metals (Pt, Ru, Ag)[14–17] and base metals (Fe, Mn, Co)[18–21], have attracted considerable research interest. Despite exhibiting efficacy in the ammoxidation of aromatic alcohols to nitriles, these catalysts frequently necessitate elevated temperatures (above 100 °C), high oxygen pressures (exceeding 5 bar), and often suffer from low reaction efficiency. This limitation is frequently attributed to strong ammonia adsorption on the metal surface[17], hindering reactant

[1]National Key Laboratory of Biobased Transportation Fuel Technology, School of Chemical Engineering, Zhengzhou University, Zhengzhou, China. [2]Key Laboratory of Biomass Chemical Engineering of Ministry of Education, College of Chemical and Biological Engineering, Zhejiang University, Hangzhou, China. [3]Shanghai Synchrotron Radiation Facility, Shanghai Advanced Research Institute, Chinese Academy of Sciences, Shanghai, China. [4]CAS Key Laboratory of Green Process and Engineering, Institute of Process Engineering, Innovation Academy for Green Manufacture, Chinese Academy of Sciences, Beijing, China. [5]Zhejiang Key Laboratory of Green Biomanufacturing of Functional Sugar Alcohols, Institute of Zhejiang University-Quzhou, Quzhou, China. [6]These authors contributed equally: Jialin Yang, Zhecheng Fang, Zhiwei Sun. ✉e-mail: nanb@sari.ac.cn; liuxl@ipe.ac.cn; rnie@zzu.edu.cn; jiefu@zju.edu.cn

activation, particularly for molecular oxygen. Furthermore, the use of harsh reaction conditions can lead to undesirable side reactions such as over-oxidation, hydrolysis, and polymerization[22], especially with biomass-derived heteroaromatic alcohols and aldehydes. Therefore, the development of a robust and environmentally benign heterogeneous metal catalyst for this transformation remains a significant challenge.

Single-atom catalysts (SACs) have garnered significant attention for dehydrogenation and oxidation reactions due to their maximized atom utilization, tunable coordination environments, and unique metal-support interactions[23,24]. Our previous work demonstrated that atomically dispersed Co-N-C catalysts exhibit superior selectivity in the room-temperature anaerobic dehydrogenation of N-heterocycles, surpassing the performance of numerous noble metal catalysts[25]. However, limitations such as weak reactant adsorption due to competitive O_2 adsorption, slow C-H/N-H bond scission kinetics, and altered reaction pathways stemming from the absence of ensemble metal sites in SACs can hinder their dehydrogenation efficiency[26]. Inspired by the potential of bimetallic Co catalysts, such as Co-Zn, Co-Cu, and CoFe[27–29], to optimize reactant adsorption configurations, break linear scaling relationships for adsorption energies of reaction intermediates, and enhance catalytic activity and selectivity[30].

Ru-based catalysts have proven effective in oxidative dehydrogenation, where partial d-electron transfer from $Ru^{\delta+}$ to supports (e.g., N-doped carbon) shifts the d-band center below the Fermi level, weakening NH_3 orbital interactions and enhancing intrinsic poisoning resistance[17]. However, maintaining the stability of these $Ru^{\delta+}$ species is critical, as they are susceptible to reduction and sintering, leading to catalyst deactivation[14]. The use of nitrogen-doped carbon (N-C) as a support has shown promise in stabilizing single metal atoms (M_1) through strong metal-nitrogen covalent bonding[31], offering a potential route to control the electronic state of the $Ru^{\delta+}$ species.

Herein, a highly active CoRu-N-C dual-atom catalyst featuring low-coordinated Co_1Ru_1 active sites bridged by a single nitrogen atom was successful synthesized, which demonstrates significantly enhanced nitrile yield and productivity in comparison to the Ru-N-C and Co-N-C single-atom catalysts. Comprehensive experimental results, augmented by density functional theory (DFT) calculations, elucidate that the exceptional performance of CoRu-N-C is predominantly attributed to the CoN_3 sites, which efficiently adsorb O_2 and facilitate the formation of superoxide radicals through electron transfer. Furthermore, the RuN_3 sites play a pivotal role in adsorbing imine intermediates. The synergistic interaction between Co and Ru promotes the cleavage of N-H and C-H bonds, thereby augmenting the overall catalytic efficiency (as illustrated in Fig. 1). Notably, the superior CoRu-N-C catalyst also demonstrates versatility, capable of being applied to the selective ammoxidation of a wide range of aromatic aldehydes, aliphatic aldehydes, and heterocyclic aldehydes, converting them into various nitriles. This underscores the multifaceted nature of the CoRu dual-atom species in heterogeneous catalysis.

Results

Catalyst characterizations

CoRu-N-C was synthesized via a support-sacrificial method (Fig. 2a). This involves the ultrasonic mixing of $Co(OAc)_2$, $Ru(acac)_3$, 1,10-phenanthroline, and $Mg(OH)_2$, followed by pyrolysis under N_2 and MgO removal[32,33]. Co-N-C was prepared similarly, omitting the Ru precursor. The ICP-AES analysis reveals Ru and Co loadings of 0.17 wt% and 3.98 wt%, respectively, in CoRu-N-C (Table S1).

XRD analysis (Fig. 2b) of CoRu-N-C, Co-N-C, and N-C reveals broad diffraction peaks at ~22° and ~45°, characteristic of the (002) and (101) planes of amorphous carbon (PDF#01-075-1621)[25]. The absence of crystalline Co, CoO_x, Ru, or RuO_x phases suggests a high degree of metal dispersion on the N-doped carbon support. Raman spectroscopy (Fig. S1) confirms the presence of analogous defective structures in all samples. Nitrogen adsorption isotherms (Fig. S2) and scanning electron microscopy (SEM) images (Fig. S3) show that Ru doping leads to an enhanced porous structure and increased BET surface area, attributing to the strong Ru-carbon/nitrogen framework interaction-induced distortion, which facilitates the formation of defective pores[34,35]. Specifically, BET surface areas are 939, 420, and 470 m^2/g, and pore volumes are 1.465, 0.464, and 0.647 cm^3/g for CoRu-N-C, Co-N-C, and N-C, respectively (Table S1).

XPS analysis (Fig. 2c–e, Table S2) reveals the chemical states of the metal species. Co 2*p* spectra indicate the presence of $Co^{\delta+}$ in both Co-N-C and CoRu-N-C, consistent with strong Co-N interactions[32]. Deconvolution of the N 1*s* spectra (Fig. S5) reveals pyridinic N (398.4 eV), pyrrolic N/M-N_x (399.8 eV), graphitic N (400.7 eV), and oxidized pyridinic N (403.3 eV). CoRu-N-C exhibits a higher intensity at 399.8 eV, suggesting an increased concentration of M-N_x species, particularly Ru-N_x resulting from Ru doping. The Ru 3*d* (Fig. 2d) and Ru 3*p* (Fig. 2e) spectra, exhibiting peaks at 280.2 eV and 461.2/486.2 eV, respectively, indicate a positive oxidation state for Ru, attributed to strong interactions with pyridinic nitrogen[32].

Aberration-corrected high-angle annular dark-field scanning transmission electron microscopy (AC-HAADF-STEM) was employed

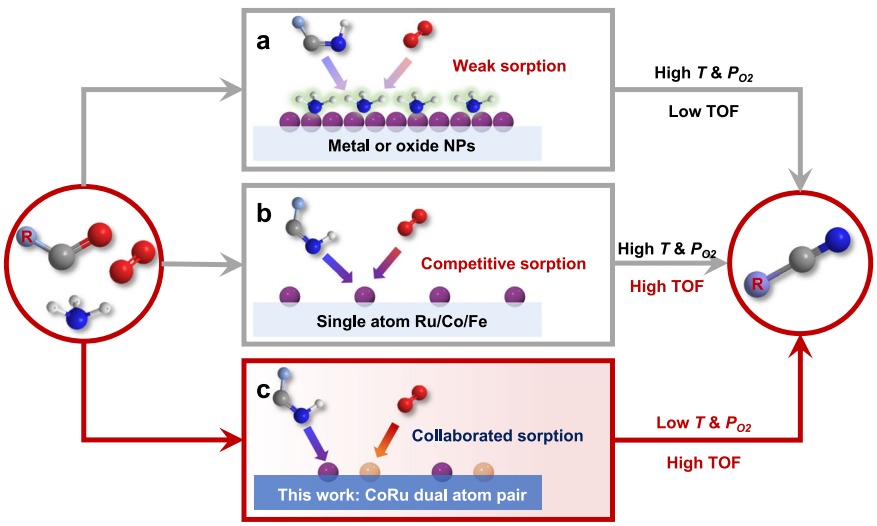

Fig. 1 | Representative works on ammoxidation of aldehydes/alcohols to nitriles. a Traditional metal or oxide nanoparticle-catalyzed ammoxidation. **b** Metal single-atom-catalyzed ammoxidation. **c** This work: Efficient ambient ammoxidation achieved using a CoRu dual single-atom catalytic material.

https://doi.org/10.1038/s41467-025-64418-7

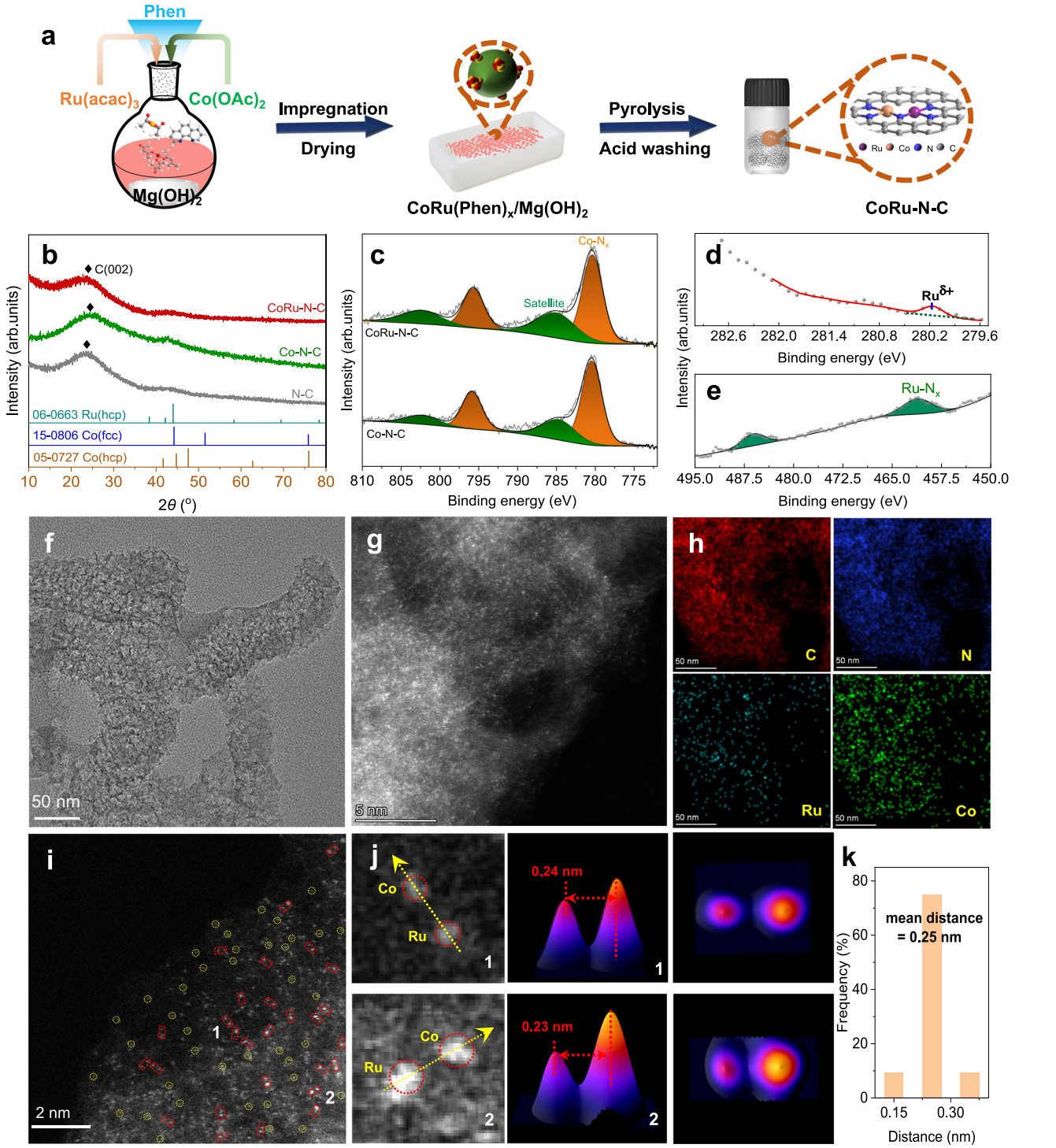

Fig. 2 | Catalyst characterization. a Schematic synthesis of CoRu-N-C catalyst. **b** XRD spectra, **c** Co 2*p* XPS spectra of CoRu-N-C, Co-N-C and N-C. **d** Ru 3*p* and **e** Ru 3*d* XPS spectra of CoRu-N-C. **f** TEM image and **g**, **i** AC HAADF-STEM images of CoRu-N-C. The dashed circles indicate single Co atoms (yellow) and the dashed boxes indicate dual atoms (red) of Co/Ru. **h** Corresponding element mapping images. **j** 3D intensity surface plot and intensity range displayed for the region 1 and region 2 in (**i**). **k** Statistical distance of dual single atoms.

to characterize the dispersion of Co and Ru within the catalyst. HRTEM images (Fig. 2f) and HAADF images reveal no nanoparticles or clusters, indicating atomic-level dispersion of the metal species. AC-HAADF-STEM image (Fig. 2g) shows a high density of uniformly bright spots on the surface of the porous carbon support. High-magnification image (Fig. 2i) reveals the presence of both isolated single atoms (highlighted by yellow dashed circles) and dual-atom sites (highlighted by red dashed boxes) in CoRu-N-C. Atomic distance measurements (Fig. 2k) across various regions confirm the formation of dual-metal sites, exhibiting a characteristic distance of 2.5 ± 0.4 Å and a distinct intensity variation along the X-Y direction consistent with the presence of Co and Ru atoms. Quantitative analysis of the bright spots (Fig. 2i, j) indicates that dual-atom sites constitute a minority of the total metal sites, consistent with the higher Co/Ru molar ratio in the catalyst. Elemental energy-dispersive X-ray spectroscopy (EDS) mapping (Fig. 2h) acquired in HAADF-STEM mode demonstrates a

https://doi.org/10.1038/s41467-025-64418-7

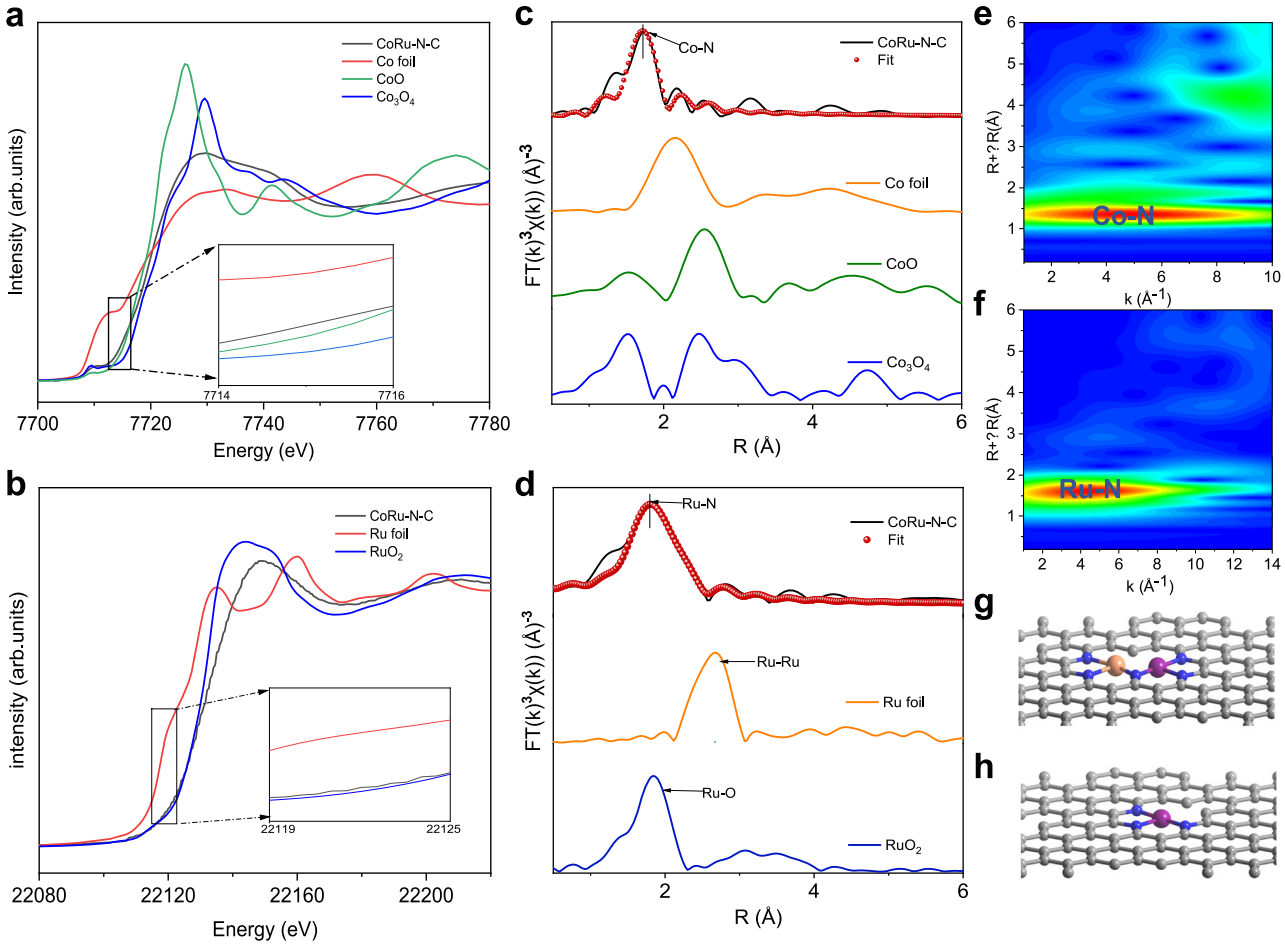

Fig. 3 | X-ray absorption spectroscopy of catalysts. XANES spectra of **a** Co K-edge, **b** Ru K-edge. **c** Co K-edge and **d** Ru K-edge EXAFS spectrum fitting of CoRu-N-C. Wavelet transform plots for **e** Co element and **f** Ru element of CoRu-N-C. Structural models of **g** CoRuN and **h** CoN moiety (the blue, gray, purple and yellow spheres present N, C, Co, and Ru atoms).

homogeneous distribution of Co and Ru throughout the carbon support. In contrast, AC-HAADF-STEM analysis of Co-N-C (Fig. S7) reveals only isolated single Co atoms, with no observable dual-atom sites.

The atomic structure of CoRu-N-C was investigated using X-ray absorption fine structure (XAFS) spectroscopy at both the Co and Ru K-edges. Normalized Co K-edge X-ray absorption near-edge structure (XANES) spectra (Fig. 3a, Fig. S10) reveal an absorption edge energy intermediate between those of Co foil and CoO, indicating a Co valence state between 0 and +2. Similarly, Ru K-edge XANES spectra (Fig. 3b) show an absorption edge between those of Ru foil and RuO_2, suggesting a Ru valence state between 0 and +4. k^3-Weighted Fourier-transform extended X-ray absorption fine structure (FT-EXAFS) spectra exhibit prominent peaks at ~1.4 Å (Co K-edge) and ~1.5 Å (Ru K-edge), assigned to Co-N and Ru-N scattering paths, respectively (Fig. 3c, d). The absence of Co-Co and Ru-Ru scattering peaks at ~2.2 Å and ~2.6 Å, respectively, confirms the isolated single-atom nature of both Co and Ru. EXAFS curve fitting analysis yields a Co coordination number of ~3 with an average bond length of 1.88 Å, consistent with a local structure of Co coordinated to three nitrogen atoms (Fig. 3c, Fig. S10, Table S3). Similarly, EXAFS fitting of the Ru K-edge data indicates a planar $Ru-N_3$ structure (Fig. 3d, Table S3). Wavelet transform (WT) analysis (Fig. 3e, f, Fig. S10c) further supports these findings, showing no evidence of metal-metal coordination at either K-edge. These results confirm the successful synthesis of a dual Co/Ru single-atom catalyst structure in CoRu-N-C (Fig. 3g, h), providing a structural basis for its catalytic activity.

Catalytic ammoxidation of FAL

The catalytic performance of various single-atom catalysts in FAL ammoxidation was evaluated under 1 bar of air at 35 °C (Fig. 4a, Table S4). A control experiment in the absence of a catalyst yields 33% imine but no FAN. Co-N-C exhibits 82% FAL conversion and 23% FAN yield, while Ru-N-C shows comparable values (76% and 25%, respectively). Although CoRu-N-C with an optimized Co/Ru ratio (0.98/0.02, Table S5) does not significantly enhance FAL conversion (88%), it leads to a substantial increase in FAN yield to 59%, demonstrating the promotional effect of Ru doping on FAN formation, which is consistent with the improved catalytic performance observed in benzyl alcohol ammoxidation (Fig. S11). In contrast, commercially available Ru/C, Pt/C, and Pd/C catalysts exhibit significantly lower FAN yields (1.9%, 8.9%, and 0.8%, respectively). Considering the metal loadings determined by ICP-OES (Table S1), the FAN productivity (at 6 h) of CoRu-N-C (47 mmol/$g_{\text{-metal}}$/h) is substantially higher than those of Ru/C (1.3 mmol/$g_{\text{-metal}}$/h), Pt/C (5.9 mmol/$g_{\text{-metal}}$/h), and Pd/C (0.5 mmol/$g_{\text{-metal}}$/h), exhibiting 36, 8, and 94-fold enhancements, respectively (Table S4), aligning with the performance differences among the catalysts normalized by metal mass (Table S6).

To elucidate the reaction pathways in FAL ammoxidation, time-dependent studies were performed over Co-N-C and CoRu-N-C (Fig. 4b, c and Fig. S12). Consistent with previous reports[10], FAL undergoes spontaneous nucleophilic substitution with ammonia to form a hemiaminal intermediate, which subsequently dehydrates to an imine. In the absence of a catalyst, both FAL conversion and imine yield

https://doi.org/10.1038/s41467-025-64418-7

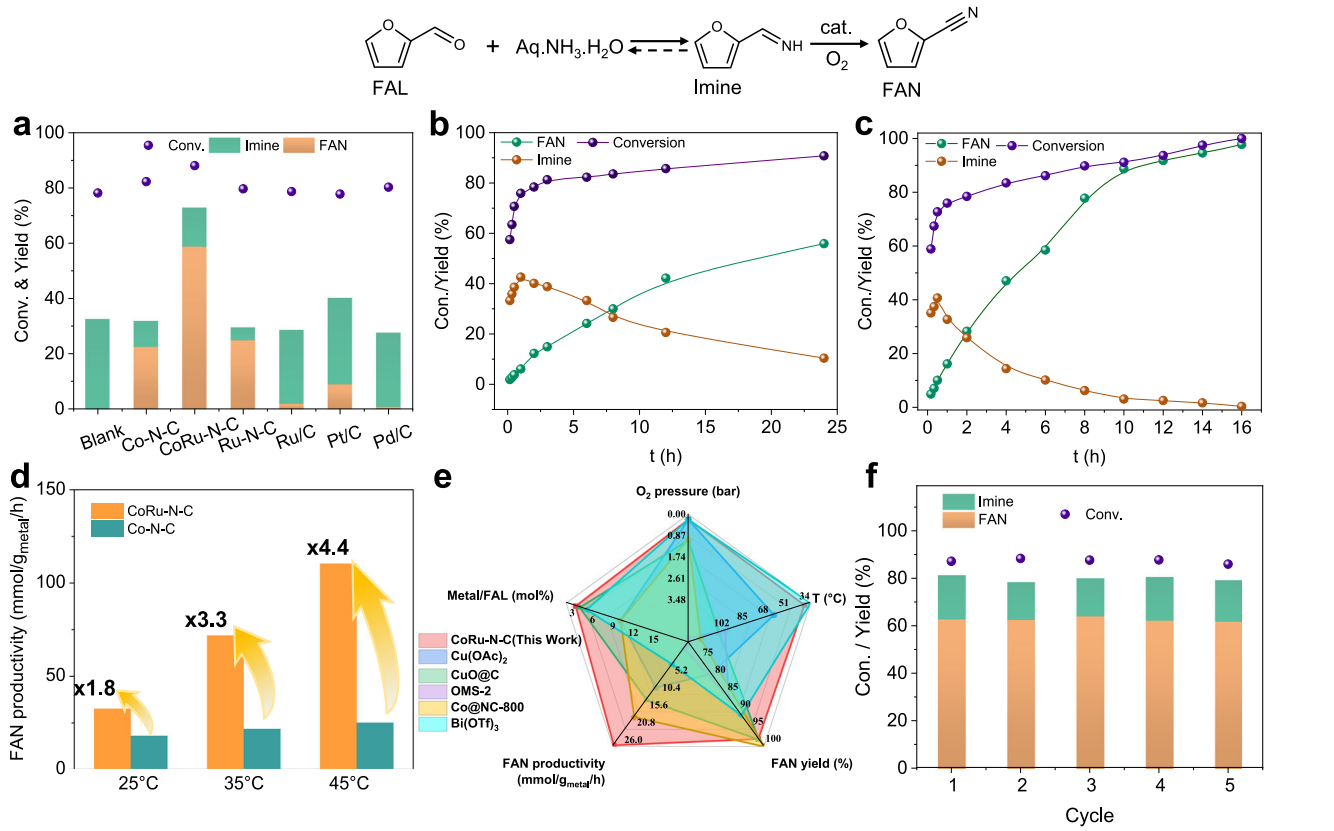

Fig. 4 | Catalytic ammoxidation of FAL. a Catalyst screen for the FAL ammoxidation. Time profiles of FAL ammoxidation over **b** Co-N-C and **c** CoRu-N-C. **d** Calculation of FAN productivity for Co-N-C and CoRu-N-C at 2 h. **e** Comparison of FAL ammoxidation of representative noble and non-noble metal catalysts. **f** Recyclability of CoRu-N-C for FAL ammoxidation. Reaction conditions: substrate (0.2 mmol), $NH_3{\cdot}H_2O$ (300 mg), CoRu-N-C (10 mg), n-butanol (1.5 mL), 35 °C, 1 bar air, 6 h.

reach plateaus of 77% and 33%, respectively, after 1 h, indicating that imine dehydrogenation is the rate-limiting and catalyst-dependent step. In the presence of Co-N-C and CoRu-N-C, the imine yield initially increases, reaching a maximum at 60 and 30 min, respectively, before gradually decreasing as FAN yield increases. After 12 h, the FAN yield reaches 94% over CoRu-N-C and 42% over Co-N-C. Extending the reaction time further results in a FAN yield of 98% for CoRu-N-C (16 h) and 56% for Co-N-C (24 h). The FAN productivity (at 2 h) of CoRu-N-C is significantly higher than that of Co-N-C at various temperatures (25, 35, and 45 °C), exhibiting 1.8, 3.3, and 4.4-fold enhancements, respectively (Fig. 4d). The catalytic performance of CoRu-N-C surpasses that of most reported homogeneous and heterogeneous catalysts for FAL or benzyl alcohol ammoxidation across various parameters, including O_2 pressure, temperature, substrate/metal molar ratio, nitrile productivity, and nitrile yield (Fig. 4e, Table S7, Table S8)[14,15,20,36–43].

The recyclability of CoRu-N-C is evaluated under conditions of low conversion to favor observing catalyst deactivation (Fig. 4f). After five consecutive reaction cycles, the catalyst exhibits negligible loss of activity, maintaining a FAN yield of ~62%. ICP analysis (Table S1) confirms the negligible Co or Ru leaching, and the constant FAN yield after catalyst removal in the hot-filtration experiment (Fig. S13) ruled out homogeneous catalysis. Furthermore, XRD (Fig. S14a), XPS (Fig. S14b-d) and XAS (Fig. S15) analyses of the recovered catalyst reveal no significant changes in its structural integrity, elemental composition, or oxidation states. These results demonstrate the high stability and reusability of the CoRu-N-C catalyst for FAL ammoxidation.

To assess the generality of the catalytic system, the activity of Co-N-C and CoRu-N-C was evaluated in ammoxidation of a range of aldehydes and alcohols (Fig. 5, Table S9). CoRu-N-C demonstrates superior catalytic performance compared to Co-N-C across various substrates, including aliphatic, polycyclic, and alkyl aldehydes. Aliphatic aldehydes selectively form nitriles, while aromatic aldehydes generate trace imines, arising from C=N bond-aromatic ring electronic and steric effects[1,44]. The most significant enhancement is observed with n-hexanal, exhibiting a 4.4-fold increase in nitrile yield (from 20% to 87%). Similarly, substantial improvements are observed for 2-naphthylacetonitrile (2.6-fold increase, from 31% to 80%) and 3-phenylpropanenitrile (3.1-fold increase, from 28% to 89%). Moderate enhancements are also observed for cyclohexanal (2.0-fold) and 5-methylfurfural (2.1-fold). Yields of thienyl-2-acetonitrile and benzyl cyanide are also increased by more than 20%. Notably, CoRu-N-C efficiently converted various benzyl alcohol derivatives into the corresponding nitriles under near-room-temperature conditions, achieving yields of 88–97% (Table S9).

Mechanism investigations

To elucidate the origin of the enhanced catalytic activity of CoRu-N-C, a series of control experiments was conducted (Fig. 6a, Table S4). A N-C support alone exhibits negligible activity, yielding only 1.2% FAN. Post-synthetic loading of Ru onto Co-N-C (Ru/Co-N-C) results in a modest improvement in FAN productivity (21 $mmol/g_{-metal}/h$), comparable to Co-N-C (19 $mmol/g_{-metal}/h$). Similarly, Ru/N-C shows minimal activity (0.2% FAN yield). These results suggest weak interaction between the post-loaded Ru and the support, hindering catalytic performance. Replacing Co with Ru in the synthesis (Ru-N-C) yielded significantly lower productivity (29 $mmol/g_{-metal}/h$) than CoRu-N-C (47 $mmol/g_{-metal}/h$). Control experiments using individual precursors ($Co(OAc)_2$, phen, or $Co(phen)_2$ yield no FAN. Furthermore, the addition of KSCN, a known poison for metal sites, results in a significant decrease in FAN yield (Fig. S16). These findings collectively strongly

https://doi.org/10.1038/s41467-025-64418-7

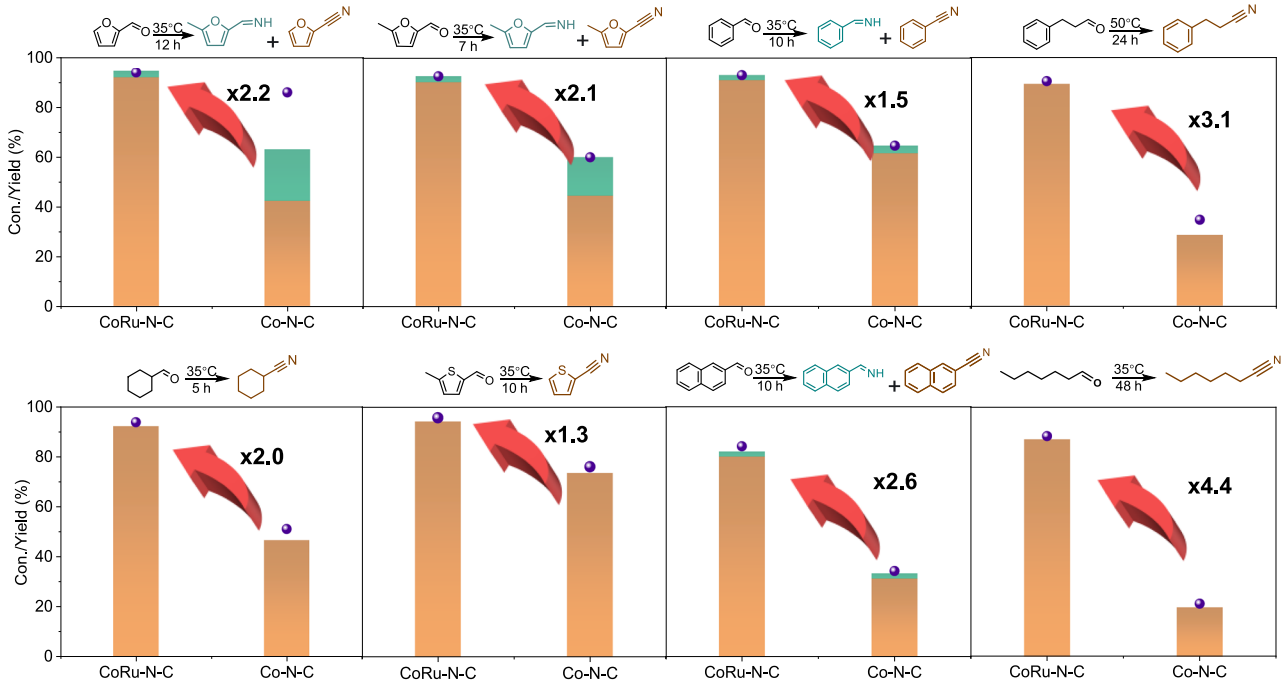

Fig. 5 | Catalytic ammoxidation of various aldehydes. Reaction conditions: substrate (0.2 mmol), $NH_3{\cdot}H_2O$ (300 mg), CoRu-N-C (10 mg), n-butanol (1.5 mL), 35 °C, 1 bar air.

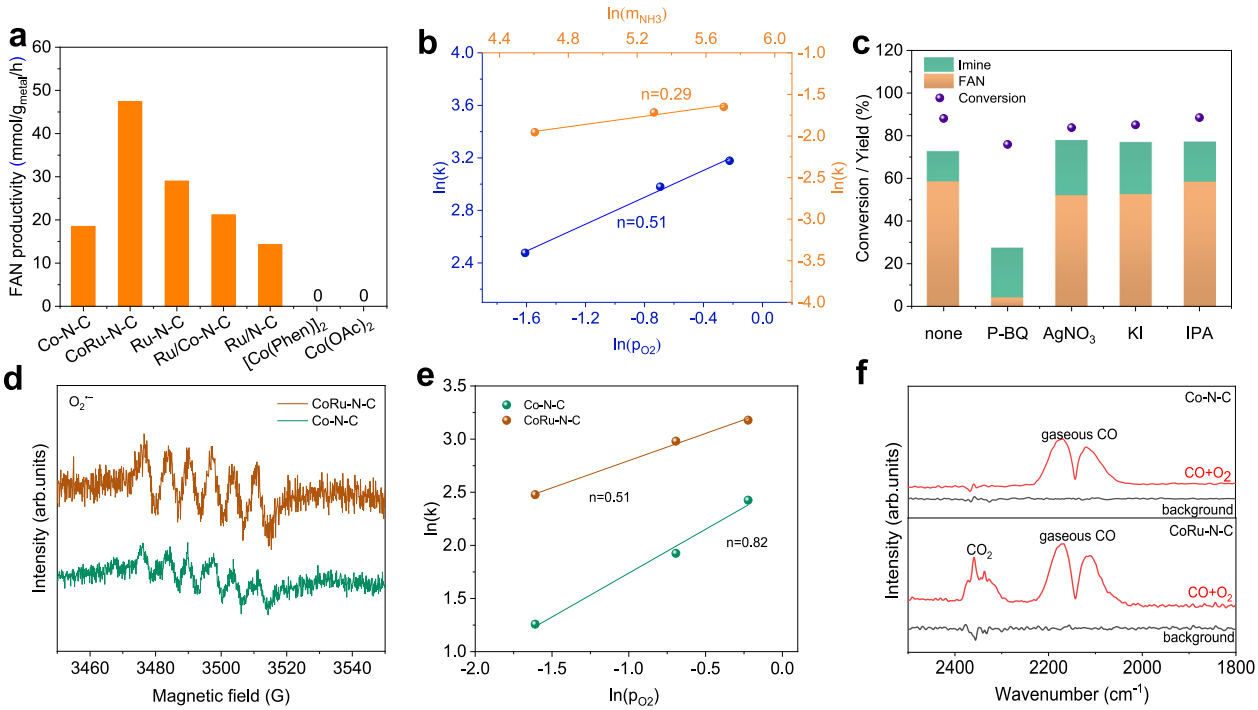

Fig. 6 | FAL ammoxidation mechanism. a Control catalysts for FAL ammoxidation. Reaction conditions: FAL (0.2 mmol), scavenger (0.2 mmol), n-butanol (1.5 mL), catalyst (10 mg), 35 °C, 1 bar air, 6 h. **b** Reaction orders of oxygen pressure and $NH_3{\cdot}H_2O$ dosage over CoRu-N-C. **c** Effect of the radical scavenger on FAL ammoxidation over CoRu-N-C. [p-benzoquinone (PBQ), superoxide radicals ($O_2^{\cdot-}$) scavenger; $AgNO_3$, photo-generated electrons (e^-) scavenger; KI, photo-generated holes (h^+) scavenger; and isopropanol (IPA), hydroxyl radicals (*OH) scavenger]. EPR spectra of radical adducts signal labeled by **d** DMPO for superoxide radicals ($O_2^{\cdot-}$) in presence of Co-N-C and CoRu-N-C. **e** Reaction orders of oxygen pressure over Co-N-C and CoRu-N-C. **f** In-situ CO oxidation over Co-N-C and CoRu-N-C.

suggest that the synergistic interaction between Co and Ru atoms, forming CoRu atom-pairs, is crucial for the superior catalytic performance observed in CoRu-N-C for FAL ammoxidation.

The significant enhancement in FAN productivity observed with CoRu-N-C suggests that overcoming the activation barrier of the rate-limiting step is crucial for achieving high reaction rates[22]. Kinetic analysis reveals a lower reaction order for $NH_3{\cdot}H_2O$ (0.29) compared to O_2 (0.51) on CoRu-N-C (Fig. 6b, Figs. S17–19), revealing that O_2 activation is a critical factor in FAN formation, despite the thermodynamic favorability of the spontaneous reaction between NH_3 and FAL[10]. Given

the inherently low reactivity of molecular oxygen, its activation via the formation of reactive oxygen species is essential[33]. Radical quenching experiments (Fig. 6c) using p-benzoquinone (PBQ) resulted in a significant decrease in FAN yield (to 4.5%), suggesting the involvement of the superoxide radical ($O_2^{-\bullet}$) as a key active species in the FAL ammoxidation. This is further supported by EPR spectroscopy (Fig. 6d), which reveals stronger DMPO-$O_2^{-\bullet}$ signals for CoRu-N-C compared to Co-N-C, indicating a higher concentration of superoxide radicals on CoRu-N-C.

To elucidate the mechanism of O_2 activation on CoRu-N-C and Co-N-C, the influence of O_2 partial pressure was examined (Fig. 6e, Fig. S19). Kinetic analysis reveals a reaction order of 0.51 for CoRu-N-C and 0.82 for Co-N-C with respect to O_2. The lower reaction order observed for CoRu-N-C indicates enhanced O_2 adsorption and activation kinetics. This is corroborated by O_2-TPD measurements (Fig. S20), showing a stronger and higher-temperature O_2 desorption peak for CoRu-N-C. Further support is provided by in situ CO-DRIFT spectroscopy (DRIFTS) (Fig. 6f), where CO_2 formation was observed at room temperature only in the presence of both CO and O_2 over CoRu-N-C, but not over Co-N-C. These findings collectively demonstrate that the paired CoRu sites facilitate O_2 activation and accelerate the rate-limiting step of the overall reaction.

AC-STEM confirmed the single-atom and dual-single-atom structures, while EXAFS fitting elucidated their local coordination environments. The reliability of EXAFS was validated by a low R-factor (≤0.02), high-quality k-range data (3–12 $Å^{-1}$), and CN ≈ 3 stability under ±20% Debye-Waller variation. Consequently, CoN_3 and CoN_3-RuN_3 models were established for the Co-N-C (d_{Co-N} = 1.841 Å) and CoRu-N-C (d_{Co-N} = 1.840 Å, d_{Ru-N} = 2.006 Å) active sites (Table S10), respectively[45–47]. DFT calculations reveal that the CoN_3 site exhibits stronger O_2 adsorption, with η^2-adsorption parallel to the carbon layer (ΔE_{ads} = −1.14 eV) energetically favored over η^1-vertical adsorption (ΔE_{ads} = −0.82 eV) (Fig. S21 and Table S11). In contrast, the CoN_4 site displays only weaker η^1-vertical O_2 adsorption (ΔE_{ads} = −0.60 eV) (Fig. S22, Table S11), rationalizing the preference for the CoN_3 site. Upon adsorption on CoN_3, Co atom transfers 0.61 electrons to the O_2 molecule, leading to O–O bond elongation to 1.37 Å and activation to an $O_2^{-\bullet}$ (Fig. S23, Table S12). Simultaneously, the imine exhibits comparable adsorption energy (ΔE_{ads} = −0.88 eV) to O_2 on CoN_3 (Fig. S24, Table S11), indicating competitive adsorption at this single site. Consequently, preferential O_2 occupancy on CoN_3 results in a substantially weaker, physical adsorption of the imine (ΔE_{ads} = −0.17 eV) (Fig. 7a, Fig. S25), thereby hindering its efficient activation.

Following the introduction of RuN_3 adjacent to CoN_3 (CoN_2(μ-N)RuN_2), the calculated O_2 adsorption energy (ΔE_{ads}) on CoN_3 (−0.85 eV) remains slightly higher than that on RuN_3 (−0.78 eV), indicating a preferential O_2 adsorption on CoN_3 (Fig. S26, Table S6). While the ΔE_{ads} of O_2 in the CoN_2(μ-N)RuN_2 model is reduced to −0.85 eV compared to isolated CoN_3 (−1.14 eV) (Fig. 7a), the charge transfer from Co atom to O_2 (0.65 e^-) and the O–O bond length (1.38 Å) remain largely unchanged (Fig. S23, Table S12), suggesting that Ru doping does not significantly impede O_2 activation to $O_2^{-\bullet}$ at the CoN_3 site. Furthermore, charge density difference analysis reveals that, in contrast to the weak physical adsorption of the imine on isolated CoN_3 (ΔE_{ads} = −0.17 eV), a strong interaction (ΔE_{ads} = −0.96 eV) occurs between the imine and RuN_3, accompanied by significant electron depletion from the C–H/N–H bonds (Fig. 7b, c), thereby facilitating bond weakening for subsequent ammoxidation. Importantly, the imine adsorption energy on CoN_3 (−0.64 eV) is considerably lower than that on RuN_3 (−0.96 eV), indicating a preferential adsorption of O_2 on CoN_3 and the imine on RuN_3. This spatial arrangement effectively mitigates competitive O_2 adsorption, preventing the inhibition of imine activation and enabling their efficient transformation in close proximity (Fig. S27, Table S11).

In situ FTIR spectroscopy, employing O_2/NH_3 purging within the reactor, was employed to monitor the ammoxidation pathway and identify key intermediates and products (Fig. 7d). Following the introduction of gaseous FAL, characteristic C=O stretching vibrations are observed at 1674 and 1720 cm^{-1}, along with C=C stretching vibrations at 1390, 1470, and 1570 cm^{-1}. After a 10-minute vacuum treatment, the C=C absorption bands persist without a significant shift, while the C=O absorption bands exhibit a shift, and a new band appears at 1670 cm^{-1}, attributed to catalyst-adsorbed C=O species. Subsequent introduction of the O_2/NH_3 gas mixture results in the disappearance of the C=O absorption bands, concomitant with the emergence of new bands assigned to a C=N stretching vibration at 1628 cm^{-1} and an N–H stretching vibration at 3334 cm^{-1}, indicative of in situ imine intermediate formation on the catalyst surface. With prolonged reaction time and increased temperature (to 100 °C at 60 min), the C=N and N–H signals gradually diminish, while a new band appears at 2236 cm^{-1}, characteristic of the C≡N stretching vibration in FAN, suggesting that the imine intermediate undergoes oxidative dehydrogenation to yield the final product.

Based on the preceding control experiments and mechanistic studies, a proposed reaction mechanism is illustrated in Fig. 7e. The reaction initiates with the spontaneous condensation of FAL and NH_3 to form a hemiaminal intermediate. Dehydration of the hemiaminal subsequently yields an imine intermediate. Concurrently, O_2 adsorbs onto the $Co^{2+}N_3$ site, generating $O_2^{-\bullet}$/$Co^{3+}N_3$ species via electron transfer from $Co^{2+}N_3$ to O_2. The imine then binds to the RuN_3 site through a nitrogen-ruthenium interaction. Subsequently, the N–H bond of the imine undergoes nucleophilic attack by the adjacent $O_2^{-\bullet}$/$Co^{3+}N_3$ species, forming a C_4H_3O-CH-N* intermediate. Simultaneously, the $O_2^{-\bullet}$ species abstracts a hydrogen atom, transforming into an OOH* species on the CoN_3 site. A subsequent C–H bond activation occurs via interaction with the OOH*-CoN_3 species, leading to the formation of a FAN* intermediate on RuN_3, which subsequently desorbs. Concomitantly, the OOH* intermediate is converted to hydrogen peroxide (H_2O_2), as illustrated in Fig. S28, which subsequently decomposes into water and regenerates half a molecule of O_2.

To gain a more profound understanding of the ammoxidation of FAL, we conducted detailed calculations of the activation energy barriers for the C–H and N–H bond cleavage steps (Tables S13–15). As depicted in Fig. 7f, Fig. S29 and Fig. S30, O2 and imine first form a co-adsorption structure on the catalyst. During the initial dehydrogenation step on CoRu-N-C (M2: C_4H_3O-CH-NH* → C_4H_3O-CH-N* + H*), the N–H bond is more readily activated compared to the C–H bond, with a bond dissociation energy barrier (ΔG_{M2}) of 1.28 eV. The liberated H* atom is subsequently captured by a nearby Co-bound O_2* species, forming an OOH* intermediate. For the second dehydrogenation step (M4: C_4H_3O-CH-N* → C_4H_3O-C-N* + H*), the calculated ΔG_{M4} is 1.38 eV, which is higher than that of the first step. The released H* atom is then captured by the OOH* intermediate, resulting in the cleavage of the O–O bond to produce one water molecule and retain one oxygen atom on the Co site, accompanied by the desorption of the C_4H_3O-C-N* product. In contrast, the dissociation ΔG values for the C–H and N–H bonds on Co-N-C are 2.18 eV and 2.53 eV, respectively, both exceeding the corresponding ΔG values on CoRu-N-C (Fig. 7f). These findings indicate the lower catalytic activity of Co-N-C, which is consistent with the experimental results (Fig. 4a).

Discussion

In summary, a highly active CoRu-N-C dual-atom catalyst featuring low-coordinated Co_1Ru_1 active sites bridged by a single nitrogen atom has been successfully synthesized. This catalyst demonstrates significantly enhanced nitrile yield and productivity in the ambient-temperature and pressure ammoxidation of aldehydes, surpassing both analogous Co-N-C and Ru-N-C single-atom catalysts, and outperforming the majority of reported noble and non-noble metal catalysts. The selective adsorption of O_2 on the CoN_3 site and imine intermediates on the RuN_3 site effectively mitigates the limitations imposed by strong imine

https://doi.org/10.1038/s41467-025-64418-7

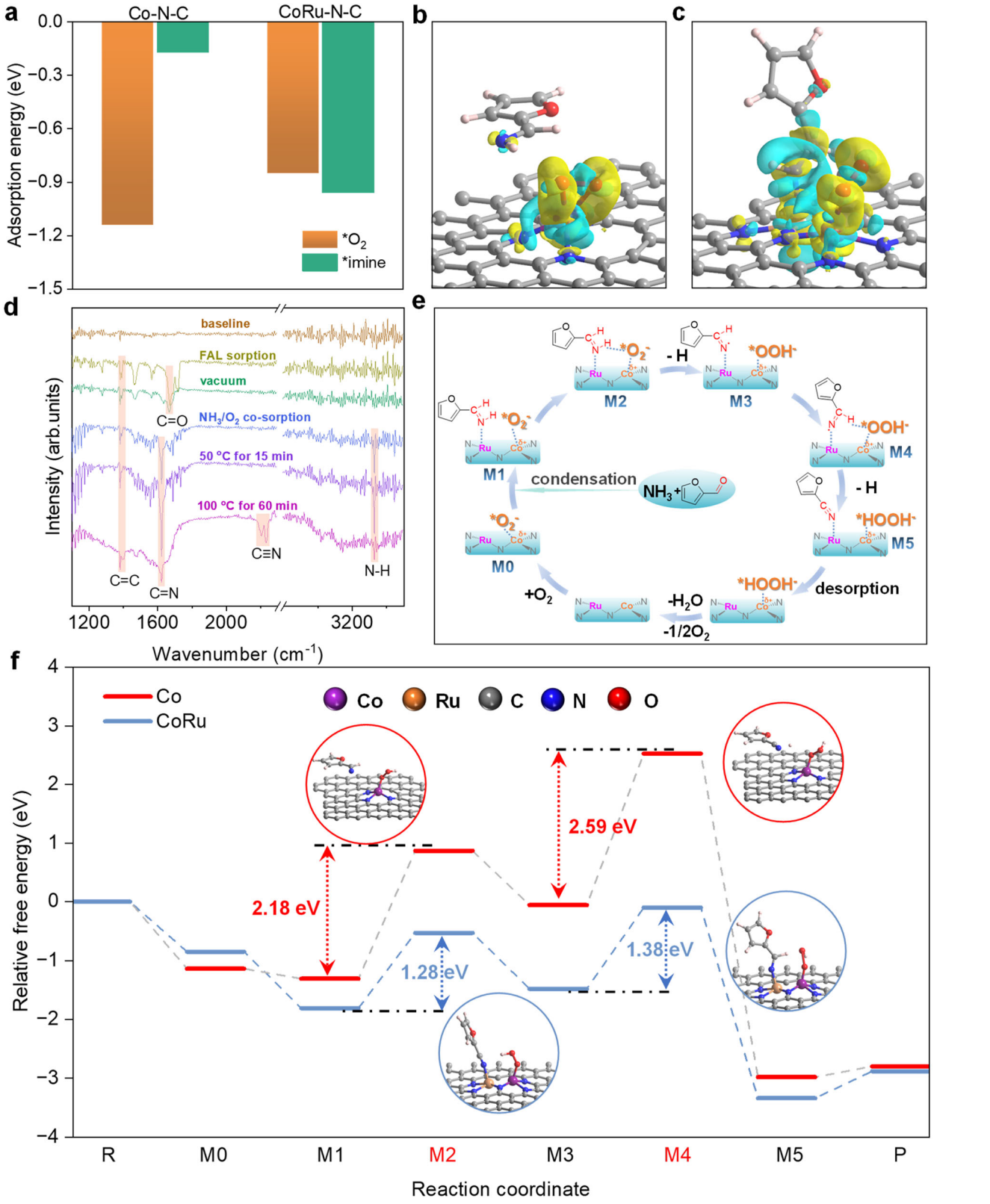

Fig. 7 | DFT study on reaction pathways and active sites. a O_2 and imine adsorption energies (ΔE_{ads}) on Co-N-C and CoRu-N-C at the most rational co-adsorption structures. The planar-average charge difference density plots of imine-adsorbed **b** Co-N-C and **c** CoRu-N-C catalysts. **d** In-situ FTIR spectra of FAL adsorbed on CoRu-N-C in the presence of NH_3 and O_2. **e** Proposed reaction mechanism for FAL ammoxidation over CoRu-N-C. **f** Energy profiles along the reaction pathway of FAL ammoxidation to FAN on Co-N-C (red) and CoRu-N-C (blue) with the intermediate structures on Co-N-C and CoRu-N-C. Color scheme: C: gray; N: blue; H: light gray; O: red; Co: purple; and Ru: orange.

adsorption, which typically hinders O_2 activation. Simultaneously, substantial electron transfer between CoN_3 and O_2 promotes the rapid formation of superoxide radicals. The close proximity of the CoN_3 and RuN_3 sites facilitates selective reactant adsorption and significantly accelerates imine oxidation and nitrile formation via a relay catalytic mechanism. These synergistic effects contribute to the exceptional catalytic activity of CoRu-N-C, exhibiting a 1.3 to 4.4-fold enhancement compared to Co-N-C. This work establishes a novel strategy for designing highly active and selective ammoxidation catalysts under mild conditions by employing precisely controlled metal atom pairs and modulating their coordination environments.

Methods

Synthesis of $Mg(OH)_2$

Specifically, 1.75 g MgO powder was dispersed in 70 mL deionized water within a 100 mL Teflon-lined stainless-steel autoclave. The sealed autoclave was maintained at 160 °C for 24 h, then allowed to cool to room temperature. The resulting suspension was filtered, washed, and dried at 80 °C overnight to yield the $Mg(OH)_2$ product.

Synthesis of CoRu-N-C, Co-N-C and Ru-N-C

In a typical synthesis, 2 mmol 1,10-phenanthroline, 0.98 mmol $Co(OAc)_2{\cdot}4H_2O$, and 0.02 mmol $Ru(acac)_3$ were dissolved in 50 mL anhydrous ethanol and stirred at room temperature for 30 min. Subsequently, 1.38 g $Mg(OH)_2$ was added, and the mixture was stirred at 60 °C for 4 h. After removal of the solvent via rotary evaporation, the solid product was dried at 80 °C under vacuum for 12 h, followed by annealing at 700 °C under a N_2 atmosphere for 2 h. Acid leaching was performed by treatment with 1 mol/L HCl for 1 h, followed by washing with copious amounts of distilled water and subsequent drying at 80 °C under vacuum for 12 h. Co-N-C, Ru-N-C, and Zn-N-C catalysts were prepared using an analogous procedure, employing 1 mmol of $Co(OAc)_2{\cdot}2H_2O$, 1 mmol $Ru(acac)_3$, and 1 mmol $Zn(OAc)_2{\cdot}2H_2O$, respectively, in place of the CoRu precursor combination.

Synthesis of Ru/Co-N-C

Specifically, 0.02 mmol $RuCl_3{\cdot}xH_2O$ was dissolved in 50 mL anhydrous ethanol, and 100 mg of Co-N-C support was added. The mixture was stirred at 60 °C for 4 h. After solvent removal via rotary evaporation, the solid was dried at 80 °C under vacuum for 12 h and subsequently annealed at 400 °C under a N_2 atmosphere for 2 h.

Synthesis of N-C

The Zn-N-C precursor was subjected to acid treatment with 8 mol/L nitric acid for 24 h, followed by thorough washing with distilled water to yield the N-C catalyst.

Synthesis of Ru/N-C

Briefly, 0.02 mmol $RuCl_3{\cdot}xH_2O$ was dissolved in 50 mL anhydrous ethanol, and 100 mg N-C support was added. The mixture was stirred at 60 °C for 4 h. Following rotary evaporation to remove the solvent, the solid was dried under vacuum at 80 °C for 12 h and subsequently annealed at 400 °C under a nitrogen atmosphere for 2 h to produce the Ru/N-C catalyst.

Catalyst characterizations

Crystal structures were determined by XRD using a PANalytical Empyrean diffractometer with Cu Kα radiation (10–90° 2θ scan range). Nitrogen adsorption-desorption isotherms at −196 °C, obtained using a Micromeritics ASAP 2460 surface area analyzer, were employed to determine the Brunauer–Emmett–Teller (BET) surface area, pore volume, pore size distribution, and average pore diameter. Prior to analysis, samples were degassed at 120 °C for 12 h. Raman spectroscopy was performed using a Renishaw instrument with an Ar-ion laser (514.5 nm excitation wavelength), acquiring spectra in the 100–4000 cm^{-1} range.

Metal loading was determined by ICP-OES using an Agilent 720ES instrument. X-ray photoelectron spectroscopy (XPS) analysis was performed on a Kratos Ultra DLD spectrometer, with binding energies referenced to the C 1s peak at 284.8 eV. Energy-dispersive X-ray spectroscopy (EDS) analysis of the Co-N-C material was conducted using a JEOL JEM-2100F field emission transmission electron microscope (TEM). Morphological characterization employed high-resolution transmission electron microscopy (HRTEM, JEOL JEM-2100F), scanning electron microscopy (SEM, ZEISS Sigma 300), and aberration-corrected high-angle annular dark-field scanning transmission electron microscopy (AC HAADF-STEM, FEI Titan Cubed Themis G2 300).

XAFS (X-ray Absorption Fine Structure) spectra of Co and Ru K edge were measured at BL16U1 and 13SSW beamline of Shanghai Synchrotron Radiation Facility (SSRF) operated at 3.5 GeV under "top-up" mode with a constant current of 200 mA[48]. The XAFS data were recorded under fluorescence mode with silicon photodiode and Lytle detector. The energy was calibrated according to the absorption edge of pure Co and Ru foil. All the catalysts were characterized by Co and Ru-K edge XANES and EXAFS in a fluorescence mode. Athena and Artemis codes were used to extract the data and fit the profiles. For the X-ray absorption near edge structure (XANES) part, the experimental absorption coefficients as function of energies μ(E) were processed by background subtraction and normalization procedures and reported as "normalized absorption" with E_0 for all the measured samples[48]. The passive electron factors, S_0^2, were determined by fitting the experimental data on Co and Ru foils and fixing the coordination number (CN) of Co-Co and Ru-Ru, and then fixed for further analysis of the measured samples.

In situ infrared (IR) spectroscopy studies of furfural (FAL) adsorption were performed using a Thermo Scientific Nicolet iS50 FTIR spectrometer. The catalyst was initially degassed at 200 °C under N_2 for 1 h, cooled to ambient temperature, and a background spectrum acquired. Following this, FAL vapor was introduced at 25 °C for 15 min, after which physisorbed FAL was removed by purging with an inert gas (15 min). Spectra were collected concurrently during the purge. A mixture of O_2 and NH_3 was then introduced, and spectra were recorded after reaction times of 10 min, 20 min, 30 min, 1 h, 1.5 h, and 2 h.

NH_3-TPD was performed using a Micromeritics AutoChem II 2920 equipped with a thermal conductivity detector (TCD). A 0.1 g catalyst sample was pretreated in a He flow at 200 °C for 1 h, cooled to 50 °C, and then exposed to 10% NH_3/Ar for 1 h. Unbound NH_3 was removed by purging with He. Desorption profiles were obtained by heating to 500 °C at a rate of 10 °C/min. O_2-TPD was conducted using an analogous procedure.

CO-DRIFTS measurements were performed using a Thermo Scientific Nicolet iS50 FTIR spectrometer. Following pretreatment at 200 °C for 1 h under inert atmosphere, the catalyst was cooled to ambient temperature and purged with Ar (15 min) to remove background adsorbates. Subsequently, CO adsorption was carried out for 15 min, followed by another Ar purge to remove physisorbed CO. Spectra were collected at 5-min intervals until no further changes in the adsorption bands were observed.

Computational methods

Spin-polarized density functional theory (DFT) calculations were performed using the Vienna Ab Initio Simulation Package (VASP 5.4.4 version)[49]. The electronic structures were determined with the Perdew–Burke–Ernzerhof (PBE) exchange-correlation functional under the generalized gradient approximation (GGA)[50]. The interaction between atomic core electrons was modeled using the projector augmented wave (PAW) method[51]. An energy cutoff of 400 eV was applied, and the force threshold for optimizing the adsorption structures was set to 0.03 eV/Å. Self-consistent field calculations were concluded when the

energy change fell below 10^{-5} eV. All calculations for Co-N-C and CoRu-N-C utilized (2 × 2 × 1) k-point grids.

To simulate the dehydrogenation process, we selected 7 × 5 graphene structure doped with three N atoms and one Co atom to construct the Co/N_3C configuration, while a model with six nitrogen atoms and combined cobalt-ruthenium atoms was created for the $CoN_2(\mu\text{-}N)RuN_2$ structure. The structures of transition states and reaction barriers for the elementary steps on all surfaces were calculated using the climbing image nudged elastic band (CI-NEB) method[52]. The Gibbs free energy of the adsorption states and the surface reaction mechanism for imine dehydrogenation were calculated under specific conditions (308 K, 0.1 MPa). More detailed computational methods are provided in the Supplementary Information.

FAL ammoxidation

Ammoxidation of FAL was conducted in a 15 mL glass tube containing 10 mg catalyst, 0.2 mmol FAL, aqueous NH_3, 1.5 mL n-butanol, and 0.2 mmol tridecane (internal standard). The reaction mixture was heated in a water bath at the desired temperature under ambient air pressure (1 bar). Following the reaction, the mixture was diluted, the catalyst removed by centrifugation, and the supernatant analyzed by gas chromatography.

Product analysis was performed using gas chromatography (GC, Fuli GC9790Plus) equipped with a flame ionization detector (FID). The GC conditions are: N_2 carrier gas, injector temperature 250 °C, detector temperature 270 °C, injection volume 0.2 μL (split ratio 20:1), and a temperature program of 50 °C (hold 5 min), 10 °C/min to 260 °C (hold 5 min). Product identification was confirmed by gas chromatography-mass spectrometry (GC-MS, Agilent 5977B) using authentic standards. FAL conversion and 2-furonitrile (FAN) yield were calculated according to the following formulas:

$$\text{Conversion}(\%) = 1 - \frac{\text{Mole of unreacted substrate}}{\text{Initial mole of substrate}} \times 100\% \quad (1)$$

$$\text{Yield}(\%) = \frac{\text{Mole of product}}{\text{Initial mole of substrate}} \times 100\% \quad (2)$$

Data availability

The data that support the findings of this study are available from the corresponding authors upon request.

References

1. Wang, C. et al. Electric field enhanced ammoxidation of aldehydes using supported fe clusters under ambient oxygen pressure. *Angew. Chem. Int. Ed.* **62**, 135–142 (2023).
2. Hu, H. et al. Recent developments in electrosynthesis of nitriles and electrocatalytic cyanations. *J. Energy Chem.* **70**, 542–575 (2022).
3. Yan, G., Zhang, Y. & Wang, J. Recent advances in the synthesis of aryl nitrile compounds. *Adv. Synth. Catal.* **359**, 4068–4105 (2017).
4. Galli, C. Radical reactions of arenediazonium ions: an easy entry into the chemistry of the aryl radical. *Chem. Rev.* **88**, 765–792 (2002).
5. Bacon, R. & Hill, H. Substitution reactions between aryl halides and cuprous salts in organic solvents. *J. Chem. Soc.* **1**, 1097–1107 (1964).
6. Anbarasan, P., Schareina, T. & Beller, M. Recent developments and perspectives in palladium-catalyzed cyanation of aryl halides: synthesis of benzonitriles. *Chem. Soc. Rev.* **40**, 5049–5067 (2011).
7. Ezawa, M. & Togo, H. One-pot preparation of C_1-homologated aliphatic nitriles from aldehydes through a wittig reaction under metal-cyanide-free conditions. *Eur. J. Org. Chem.* **10**, 2379–2384 (2017).
8. Chen, X., Song, S., Li, H., Gozaydin, G. & Yan, N. Expanding the boundary of biorefinery: organonitrogen chemicals from biomass. *Acc. Chem. Res.* **54**, 1711–1722 (2021).
9. Kasmuri, N., Kamarudin, S., Abdullah, S., Hasan, H. & Som, A. Process system engineering aspect of bio-alcohol fuel production from biomass via pyrolysis: an overview. *Renew. Sust. Energ. Rev.* **79**, 914–923 (2017).
10. Sun, K., Shan, H., Neumann, H., Lu, G. & Beller, M. Efficient iron single-atom catalysts for selective ammoxidation of alcohols to nitriles. *Nat. Commun.* **13**, 29074–29083 (2022).
11. Yin, W., Wang, C. & Huang, Y. Highly practical synthesis of nitriles and heterocycles from alcohols under mild conditions by aerobic double dehydrogenative catalysis. *Org. Lett.* **15**, 1850–1863 (2013).
12. Botta, C. et al. Polymorphism-dependent aggregation-induced emission of a push–pull dye and its multi-stimuli responsive behavior. *J. Mater. Chem. C.* **4**, 2979–2989 (2016).
13. Dighe, S., Chowdhury, D. & Batra, S. Iron nitrate/TEMPO: a superior homogeneous catalyst for oxidation of primary alcohols to nitriles in air. *Adv. Synth. Catal.* **356**, 3892–3896 (2014).
14. Oishi, T., Yamaguchi, K. & Mizuno, N. Catalytic oxidative synthesis of nitriles directly from primary alcohols and ammonia. *Angew. Chem. Int. Ed.* **48**, 6286–6288 (2009).
15. Preger, Y., Root, T. & Stahl, S. Platinum-based heterogeneous catalysts for nitrile synthesis via aerobic oxidative coupling of alcohols and ammonia. *ACS Omega* **3**, 6091–6096 (2018).
16. Hashemi, A. N., Eshghi, H. & Lamei, K. Uniform silver nanoparticles on tunable porous N-doped carbon nanospheres for aerobic oxidative synthesis of aryl nitriles from benzylic alcohols. *Appl. Organomet. Chem.* **33**, 4835–4844 (2019).
17. Wang, H. et al. Atomically dispersed Ru on manganese oxide catalyst boosts oxidative cyanation. *ACS Catal.* **10**, 6299–6308 (2020).
18. Jagadeesh, R. V., Junge, H. & Beller, M. Green synthesis of nitriles using non-noble metal oxides-based nanocatalysts. *Nat. Commun.* **5**, 4123–4132 (2014).
19. Sun, K., Sun, J., Lu, G. & Cai, C. Enhanced catalytic activity of cobalt nanoparticles encapsulated with an N-doped porous carbon shell derived from hollow ZIF-8 for efficient synthesis of nitriles from primary alcohols in water. *Green. Chem.* **21**, 4334–4340 (2019).
20. Wang, H., Luo, Q. & Wang, L. Product selectivity controlled by manganese oxide crystals in catalytic ammoxidation. *Chin. J. Catal.* **42**, 2164–2172 (2021).
21. Murugesan, K., Senthamarai, T. & Sohail, M. Stable and reusable nanoscale Fe_2O_3-catalyzed aerobic oxidation process for the selective synthesis of nitriles and primary amides. *Green. Chem.* **20**, 266–273 (2018).
22. Xian, C. et al. High nitrile yields of aerobic ammoxidation of alcohols achieved by generating $^{\bullet}O_2^-$ and $Br^{\bullet}$ radicals over iron-modified TiO_2 photocatalysts. *J. Am. Chem. Soc.* **144**, 23321–23331 (2022).
23. Qiao, B. et al. Single-atom catalysis of CO oxidation using Pt_1/FeO_x. *Nat. Chem.* **3**, 634–641 (2011).
24. Shi, J. et al. Introducing Co-O moiety to Co-N-C single-atom catalyst for ethylbenzene dehydrogenation. *ACS Catal.* **12**, 7760–7772 (2022).
25. Li, Q. et al. Acceptorless ambient-temperature dehydrogenation and reversible hydrogenation of N-heterocycles over single-atom Co-N-C catalysts. *Appl. Catal. B Environ.* **351**, 23959–23970 (2024).
26. Huang, F. et al. Low-temperature acetylene semi-hydrogenation over the Pd_1-Cu_1 dual-atom catalyst. *J. Am. Chem. Soc.* **7**, 18485–18493 (2022).
27. Chai, Y. et al. Dual-atom catalyst with N-colligated Zn_1Co_1 species as dominant active sites for propane dehydrogenation. *J. Am. Chem. Soc.* **146**, 263–273 (2023).
28. Shi, Y. et al. Atomically dispersed cobalt/copper dual-metal catalysts for synergistically boosting hydrogen generation from formic acid. *Angew. Chem. Int. Ed.* **135**, 13099–13110 (2023).
29. Liu, C. et al. Catalytic activity enhancement on alcohol dehydrogenation via directing reaction pathways from single- to double-atom catalysis. *J. Am. Chem. Soc.* **144**, 4913–4924 (2022).

30. Li, L., Yuan, K. & Chen, Y. Breaking the scaling relationship limit: from single-atom to dual-atom catalysts. *Acc. Mater. Res.* **3**, 584–596 (2022).
31. Tian, S. et al. High-loading single-atomic-site silver catalysts with an Ag_1-C_2N_1 structure showing superior performance for epoxidation of styrene. *ACS Catal.* **11**, 4946–4954 (2021).
32. Liu, W. et al. Single-atom dispersed Co-N-C catalyst: structure identification and performance for hydrogenative coupling of nitroarenes. *Chem. Sci.* **7**, 5758–5764 (2016).
33. Liu, W. et al. Discriminating catalytically active FeN_x species of atomically dispersed Fe-N-C catalyst for selective oxidation of the C-H bond. *J. Am. Chem. Soc.* **139**, 10790–10798 (2017).
34. Zhu, Y. et al. Supported ruthenium single-atom and clustered catalysts outperform benchmark Pt for alkaline hydrogen evolution. *Adv. Mater.* **35**, 2301133–2301141 (2023).
35. Park, K. & Lee, K. Effects of the chemical states of N sites and mesoporosity of N-doped carbon supports on single-atom Ru catalysts during CO_2-to-formate conversion. *Appl. Catal. B Environ.* **346**, 123751–123765 (2024).
36. Sridhar, M. et al. Acetohydroxamic acid: a new reagent for efficient synthesis of nitriles directly from aldehydes using $Bi(OTf)_3$ as the catalyst. *Tetrahedron Lett.* **53**, 3421–3424 (2012).
37. Das, A. K., Nandy, S. & Bhar, S. $Cu(OAc)_2$ catalysed aerobic oxidation of aldehydes to nitriles under ligand-free conditions. *RSC Adv.* **12**, 4605–4614 (2022).
38. Senthamarai, T. et al. Cu-Oxide Nanoparticles catalyzed synthesis of nitriles and amides from alcohols and ammonia in presence of air. *Adv. Sustain. Syst.* **6**, 263–272 (2022).
39. Jia, X. & Ma, J. Alkali α-MnO_2/Na_xMnO_2 collaboratively catalyzed ammoxidation-Pinner tandem reaction of aldehydes. *Catal. Sci. Technol.* **6**, 7429–7436 (2016).
40. Pan, L. & Fu, W. Highly dispersed Co species in N-doped carbon enhanced the aldehydes ammoxidation reaction activity. *Mol. Catal.* **518**, 112087–112097 (2022).
41. Jiang, X. & Wang, W. Solvent-free direct aerobic photocatalytic ammoxidation of benzyl alcohol to benzonitrile on In_2O_3/Au/POCN. *J. Catal.* **442**, 115861–115873 (2025).
42. Wang, W. et al. Direct oxidative cyanation of alcohol to nitrile over CoO_x/MnO_2 with aqueous ammonia. *ACS Sustain. Chem. Eng.* **10**, 14636–14647 (2022).
43. Liu, X. et al. Manganese carbodiimide (MnNCN): a new heterogeneous mn catalyst for the selective synthesis of nitriles from alcohols. *Angew. Chem. Int. Ed.* **64**, 13799–13809 (2024).
44. Senthamarai, T. et al. A "universal" catalyst for aerobic oxidations to synthesize (hetero)aromatic aldehydes, ketones, esters, acids, nitriles, and amides. *Chem* **8**, 508–531 (2022).
45. Lili, H., Wei, L. & Jun, S. Design of Ru-Ni diatomic sites for efficient alkaline hydrogen oxidation. *Sci. Adv.* **8**, 3799–3809 (2022).
46. Shao, S. et al. Electron-rich ruthenium single-atom alloy for aqueous levulinic acid hydrogenation. *ACS Catal.* **11**, 12146–12158 (2021).
47. Wang, X. et al. Regulation of coordination number over single Co sites: triggering the efficient electroreduction of CO_2. *Angew. Chem. Int. Ed.* **57**, 1944–1948 (2018).
48. Tai, R. & Zhao, Z. Overview of SSRF phase-II beamlines. *Nuclear Sci. Tech.* **35**, 1–10 (2024).
49. Kresse, G. & Furthmüller, J. Efficient iterative schemes for ab initio total-energy calculations using a plane-wave basis set. *Phys. Rev. B* **54**, 11169–11186 (1996).
50. Perdew, J. P., Kieron, B. & Matthias, E. Generalized gradient approximation made simple. *Phys. Rev. Lett.* **77**, 3865–3868 (1996).
51. Kresse, G. & Joubert, D. From ultrasoft pseudopotentials to the projector augmented-wave method. *Phys. Rev. B* **59**, 1758–1775 (1999).
52. Henkelman, G., Uberuaga, B. & Jónsson, H. A climbing image nudged elastic band method for finding saddle points and minimum energy paths. *J. Chem. Phys.* **113**, 9901–9904 (2000).

Acknowledgements

The authors acknowledge the financial support from the NSFC (22478366, 22425801, U23A20124), the Science and Technology Development Plan Joint Fund Project of Henan province (232301420048), the Program of Processing and Efficient Utilization of Biomass Resources of Henan Center for Outstanding Overseas Scientists (GZS2022007), and the Science and Technology Innovation Plan of Shanghai Science and Technology Commission (23YF1453700). We thank the Shanghai Synchrotron Radiation Facility of BL16U1 and 13SSW for the assistance with XAFS measurements.

Author contributions

R.N. conceptualized this work. R.N. and J.F. guided this work. R.N., X.L., and J.F. designed the experiments. J.Y. and Z.S. performed the catalyst preparation and ammoxidation. Z.F. performed the DFT calculations. B.N. performed the XAS characterizations. J.Y., Z.S., W.Z., Z.M., and Z.F. wrote the paper. R.N., X.L., B.N., and J.F. revised the manuscript. All the authors participated in the data analysis and commented on the manuscript. These authors contributed equally: J.Y., Z.F. and Z.S.

Competing interests

The authors declare no competing interests.

Additional information

Supplementary information The online version contains supplementary material available at https://doi.org/10.1038/s41467-025-64418-7.

Correspondence and requests for materials should be addressed to Bing Nan, Xiaolong Liu, Renfeng Nie or Jie Fu.

Peer review information *Nature Communications* thanks Vladislav Ivanistsev, who co-reviewed with Ritums Cepitis, and the other, anonymous, reviewer(s) for their contribution to the peer review of this work. A peer review file is available.